Final Technical Report

United States Geological Survey
Grant G09AP00086

Using Microstructures in Pulverized Rock to Constrain Dynamical Earthquake Source Models

Principal Investigator

Charles G. Sammis
Professor of Geophysics
University of Southern California
3651 Trousdale Parkway
ZHS 107
Los Angeles, CA 90089-0742
213-740-5836; 213-740-0011 (fax), e-mail: sammis@usc.edu

Period of Performance: July 1, 2009 to June 30, 2010

October 2010

Using Microstructures in Pulverized Rock to Constrain Dynamical Earthquake Source Models

Abstract

The objective of this study was to characterize the orientation of meso-scale shear localizations in “pulverized rock” adjacent to the core of large faults, and use these orientations to test the hypothesis that the rock has been pulverized in the stress concentration at the rupture tip of an earthquake. In specific we compared the observed orientations with those predicted by the dynamic slip-pulse model developed by Rice et al. [2005]. We focused on the pulverized rocks adjacent to the Sierra Madre fault in La Canada and measured the geometry and slip vectors of 115 cm-scale slip surfaces in the granitic hanging-wall. At the microscale, we identified two dominant fracture orientations. The first appears both near and far from the fault and is compatible with Andersonian failure on the main fault. The second appears only within meters from the fault and may be associated with the formation of the cm-scale slip surfaces. Characterization of damage fabric in the microscale suggests that in-situ shattering of crystals with minimal strain immediately above the fault plane may be associated with local tension possibly due to an opening mode of rupture. We conclude that the architecture of the slip surfaces was developed over a finite displacement history with fairly stable faulting conditions, and that with continuing displacement, as the rock mass approached the surface, a dynamic opening mode could have led to the observed shattering of crystals in the immediate vicinity of the slip zone.

The geometry of slip surfaces in the hanging-wall of the Sierra Madre fault, La-Canada, California: evidence for Mohr-Coulomb failure induced by a dynamic off-fault stress field.

Ory Dor[1,2], Charles G. Sammis[1], Yehuda Ben-Zion[1]

1) Department of Earth Sciences, University of Southern California, Los Angeles, CA 90089-0740, USA.
2) Currently at the Department of Geological Sciences, Brown University, Providence, RI, 02906, USA.

Abstract

An analysis of fault-slip data measured on 115 cm-scale slip surfaces in the granitic hanging-wall of the Sierra Madre fault indicates that their geometry and slip vectors match predictions of off-fault Mohr-Coulomb slip in the stress field of a propagating mode II earthquake rupture (Rice et al., 2005). At the microscale, we identified two dominant fracture orientations. The first appears both near and far from the fault and is compatible with Andersonian failure on the main fault. The second appears only within meters from the fault and may be associated with the formation of the cm-scale slip surfaces. Characterization of damage fabric in the microscale suggests that in-situ shattering of crystals with minimal strain immediately above the fault plane may be associated with local tension possibly due to an opening mode of rupture. We conclude that the architecture of the slip surfaces was developed over a finite displacement history with fairly stable faulting conditions, and that with continuing displacement, as the rock

mass approached the surface, a dynamic opening mode could have led to the shattering of crystals in the immediate vicinity of the slip zone.

Introduction

The exposure of the Sierra Madre fault on the banks of the Arroyo Seco Canyon in La Canada, California, provides a rare window into the internal structure of a major active thrust fault capable of generating large earthquakes (Rubin et al. 1998). The Cretaceous granitic hanging-wall of the fault is separated from the Pleistocenic conglomeratic footwall by an mm to a few cm wide gouge layer. The hanging wall contains a myriad of cm scale slip surfaces having a conjugate geometry. These surfaces have inclinations larger than that of the fault surface, and are observed up to a distance of several meters from it. A layer of granite containing those slip surfaces about a meter wide immediately adjacent to the slipping zone is pulverized. Since this is a seismically active fault with a known tectonic history, these damage elements, described in detail below, may be interpreted in terms of damaging mechanisms associated with the propagation of earthquake ruptures. We have identified two classes of models that discuss the dynamic generation of damage elements of the type we observe. Each makes distinct predictions about the geometry of damage produced in the vicinity of a propagating rupture front which we test here by detailed mapping, structural analysis and microscale damage fabric characterization.

The first class of models is relevant specifically to thrust faults and emphasizes an opening mode with a complete reduction of normal stress during the passage of the rupture. Following experimental work (e.g. Brune, 1996) in which fault-opening waves

were observed, especially in the fault toe, Shi et al. (1998) constructed a 2D solid lattice model of a thrust fault, showing that the rupture process is associated with a pulse of normal opening displacement. Separation of the bounding blocks occurs (Figure 1a) with a fault-normal component of opening larger in the hanging wall and complete reduction of the shear stress. An asymmetric response between the footwall and the hanging with a drop of the normal stress potentially to zero was observed in the 2D finite element modeling of Oglesby et al. (1998; 2000). These results require that rocks adjacent to the fault surface, mainly in the hanging-wall, will experience absolute tensile stresses during the passage of ruptures. Dynamic tensile regime should generate isotropic expansion of the rock resulting in a randomly oriented population of joints and minimal distortion of the rock fabric.

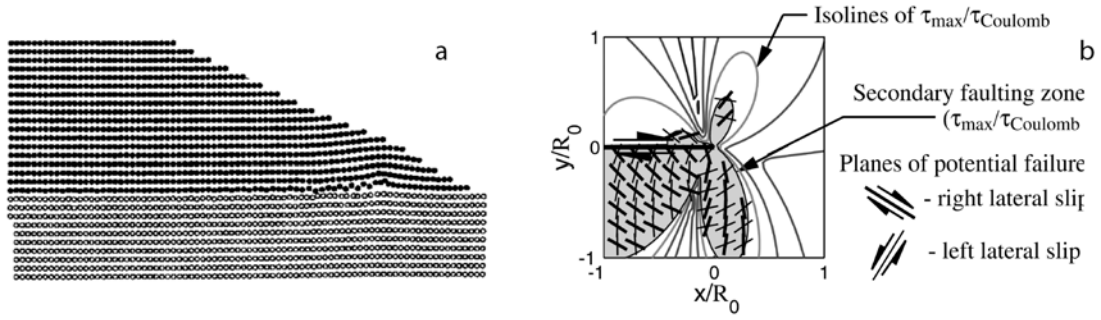

Figure 1: Model predictions. a. Figure 6a of Shi et al. (1998) showing a snapshot of typical particle motion pattern in a 2D lattice model. The rupture propagates up-dip with a pulse-like behavior and fault normal displacement in the hanging-wall larger than in the footwall, leading to fault separation. b. Figure 10b of Poliakov et al. (2002). A generic illustration of normalized shear stress isolines and expected geometry of slip surfaces used by Rice et al. (2005) to display their model results.

The second class of models discusses the stress field near the tip of a propagating rupture and its explicit role in the generation of off-fault damage. Rice et al. (2005) showed that a slip-weakening rupture front with a self-healing slip pulse can cause Mohr-Coulomb failure on cohesionless slip surfaces in the wall rock. For mode II ruptures, the area in which the failure criterion is exceeded on the hanging wall of a thrust fault during

up-dip rupture propagation, increases with rupture velocity, strength drop, poroelastic Skempton coefficient and with a smaller angle between the maximum pre-stress direction and the fault. Slip occurs by the activation of a favorably oriented conjugate set of slip surfaces with strike parallel to the main fault and with various inclination angles with respect to the fault (Figure 1b).

We performed detailed structural mapping of 115 small slip surfaces, measured the preferred orientation of microfractures and characterized microscale damage fabric in order to test which of the two sets of predictions compares most favorably with the type of damage observed in the exposed fault zone. We find that the geometry and kinematics of the slip surfaces is compatible with Mohr-Coulomb failure within the stress field induced by ruptures propagating on this fault (Rice et al., 2005), and that the pulverization immediately above the fault plane could possibly be related to dynamic fault opening. The two mechanisms require very different dynamic off-fault stresses and are not likely to operate simultaneously. Therefore, if dynamic fault opening did occur in addition to the activation of the observed slip surfaces, it represents a separate stage in the mechanical development of the fault or it corresponds to a different depth.

Regional geological setting

The Sierra Madre fault zone comprises a series of reverse faults extending more than 75 km along the southern margins of the San Gabriel Mountains (Figure 2). These are convex-southward faults which separate the crystalline pre-Tertiary rocks on the north from the Tertiary and Quaternary sedimentary formations on the south. The faults are discontinuous, with dips ranging from 30º to sub-vertical. All the segments dip northward with the crystalline rocks thrust upward toward the south over sediments as young as the

mid-Pleistocene Pacoima Formation (Oakeshott, 1971). The reverse slip along the branches of the Sierra Madre fault zone is responsible for uplift of the San Gabriel Mountains to elevations of 2-3 km and is thought to began about 7 million years ago (Blythe et al., 2000). Paleoseismological investigations suggest that the Sierra Madre fault ruptures during very infrequent, large-magnitude (M_W =>7) earthquakes (Rubin et al. 1998; Tucker and Dolan, 2001).

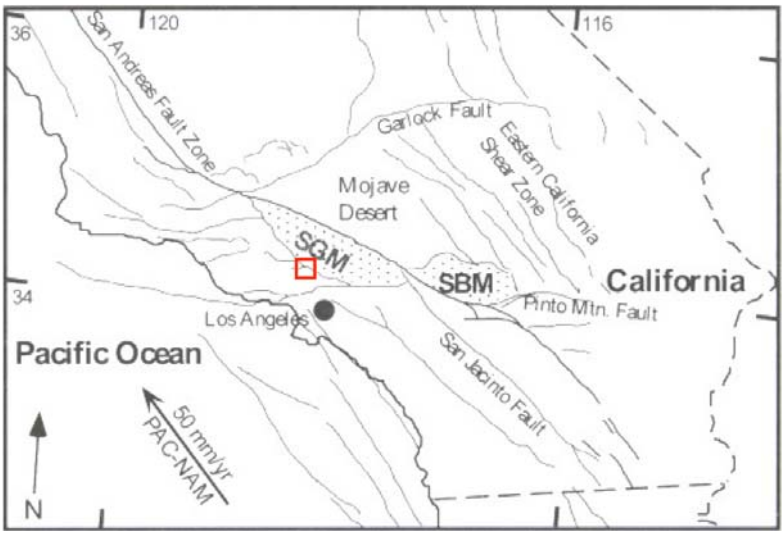

Figure 2: Location of the working site near La-Canada, California, at the foothills of the San Gabriel Mountains (SGM) along the Sierra Madre fault (thin line bounding the SGM on their southwest side. SBM – San Bernardino Mountains).

Local geological setting

The upper most tip of the Sierra Madre fault appears close to the mouth of the Arroyo Seco Canyon immediately east of the Jet Propulsion Laboratory (Figure 3). Trench studies in the vicinity of the bridge exposure found no evidence of slip during the Holocene (Crook et al., 1987), but the recurrence interval of earthquakes on the fault was found to be at the order of several thousands of years so the lack of evidence for Holocene activity does not imply that the fault is inactive. The location of the fault at the slope break at base of the mountain front indicates that this is one of the active strands

responsible for the current uplift. The minimum vertical throw on this fault strand was estimated using surface and borehole data to be 244 m (Crook et al. 1981). At this location the fault juxtaposes Cretaceous granite over a Pleistocene alluvial fan and crops out only about a meter above the bottom of the canyon channel on its east and west banks (see Figure 5).

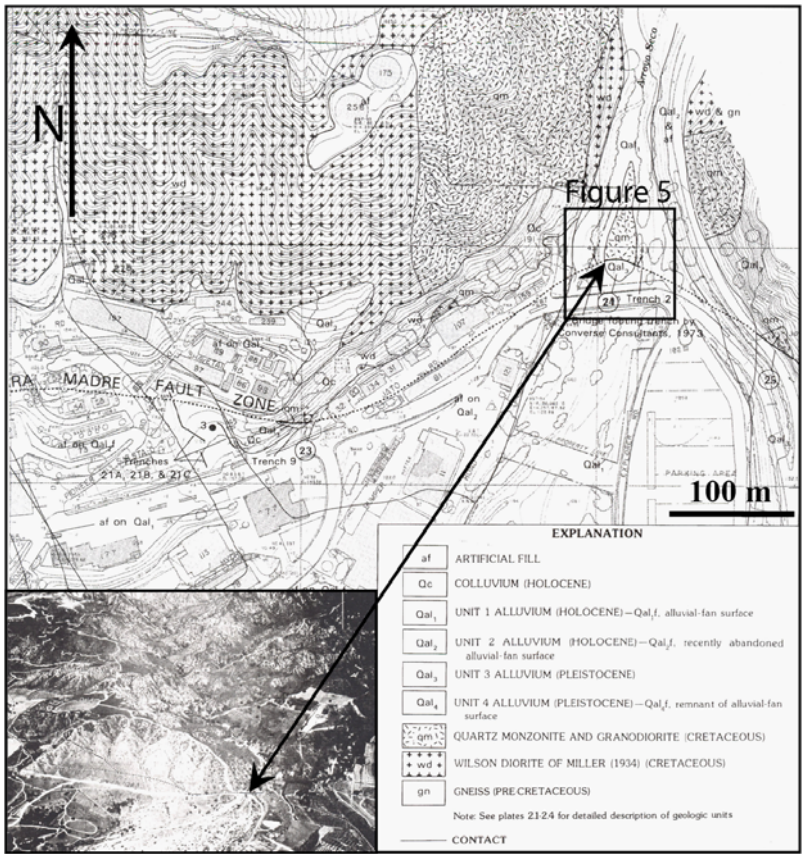

Figure 3: Geology of the Arroyo Seco canyon at its mouth. Aerial photo shows the same general area in an oblique view. The Sierra Madre Fault is marked by black continuous line where surface trace is known and with dotted line where trace is projected. Arrow connects the location of the study site in the geological map and in the picture. Note contact between granite and Pleistocene unit. The photo was taken in 1934, when the area was not populated yet. Picture and map from Crook et al. (1987).

Methodology

Field mapping: The granite in the hanging-wall is dissected by a web of small slip surfaces 2-15 cm wide. These slip surfaces are the dominant and also the smallest visible structural elements in the damage zone. In order to characterize their geometry and

kinematics we measured the orientation of 115 such slip surfaces. Blocks bounded by those surfaces were removed progressively to expose more surfaces. Where possible, we recorded the plunge (inclination) and trend (azimuth) of their slip striations.

A more challenging task was the determination of the sense of slip on the surfaces based on the morphology and other properties of the striations. We used an updated classification of kinematic indicators by Doblas (1998) to determine the sense of motion on a fault if the striations on the surface contained the required information. Figure 4 shows three kinematic indicators that were used as criteria for determination of the sense of slip. These include small steps or "pull-aparts" on the fault plane (4a); "V" or crescent-shape markers (4b); and smeared dark grains (4c). We were able to determine the sense slip on 49 of the 115 surfaces.

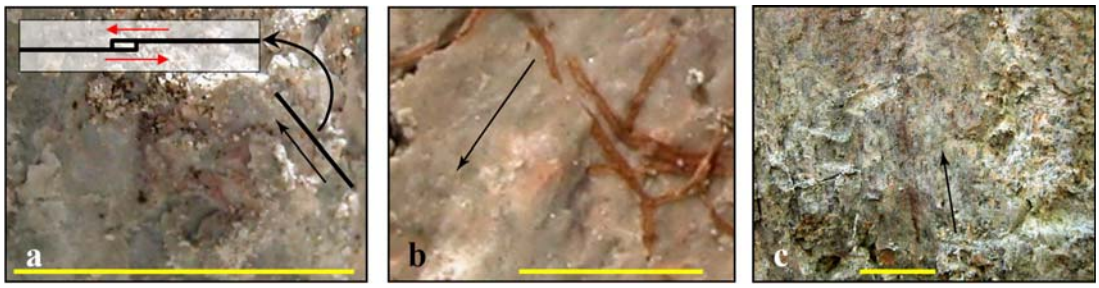

Figure 4: kinematic indicators used in this study. Yellow bars are cm long. Arrows indicate the inferred sense of motion a. Step-overs - small pull-aparts that indicate movement in the direction of the step. The cartoon shows a cross section perpendicular to the surface along the thick black line. b. Crescentic marker, indicating motion of the missing block to the direction opposite to the tip of the marker. c. Smeared grain, shows that the missing block moved upward in this case. It also shows that motion did not change sense over time as the grain is smeared only in one direction.

Microstructural analysis: we collected 6 oriented samples at horizontal distances of 0, 1, 2, 5.5, 13.3 and 250 m from the fault, corresponding to fault-normal distances of 0, 0.7, 1.5, 4, 9.7 and 183 m (assuming a sub-surface fault inclination of 47°, the dip measured in the outcrop). The fault normal distances were used to name the samples.

Sample 0 contains 2-4 mm wide gouge layer in contact with damaged granite. It was cut into three mutually perpendicular oriented thin sections. One oriented thin section was prepared from each of the other samples. We measured the orientation of transgranular microfractures in samples 4 and 183. Fractures were mostly straight or slightly curved, and for the purpose of orientation analysis could be approximated as straight lines. We compare properties of the damage fabric between these two samples and sample 0, and discuss the fault-normal variations in damage properties based on observations from all the samples.

Observations

Mesoscale observations

Figure 5 shows the local geometry of the outcrop. The fault is exposed on the banks of the south-flowing channel of the Arroyo Seco canyon immediately north of a bridge above the canyon. The dip is 47° to the northwest (334°). The gouge that separates the granitic hanging-wall from the conglomeratic foot-wall is one mm to 5 cm wide (Figure 6). It ranges from brown to almost white in places, foliated, with parallel flexible clayey slabs. Slip striations within the gouge layer have an average rake of -52E (hade = 218), suggesting oblique thrust fault motion.

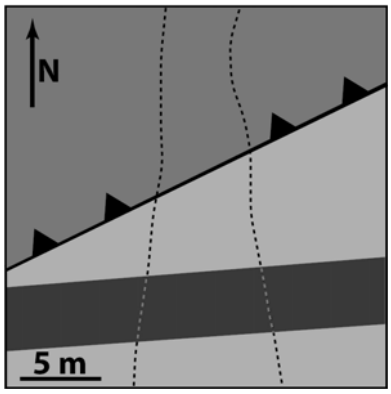

Figure 5: Local geological settings in the mapping site: dark gray – granite; light gray – alluvium. Line with triangles mark the Sierra Madre fault, triangles point in the direction of the hanging-wall. The channel of the Arroyo Seco canyon is marked with doted lines and the bridge above the canyon connecting JPL and a parking lot is marked with a thick gray bar across the map.

A 0.5-1 m wide layer of granite immediately above the fault plane appears to be pulverized (e.g. Dor et al., 2006b). Grain boundaries and other delicate magmatic fabrics are largely preserved although the rock within this layer yields a powdery texture when squeezed between two fingers. Above this layer the rock hardens over a distance of about a meter or less. Starting immediately above the gouge layer, a web of small scale slip surfaces and veins dissect the rock. Their density is the largest in the 1-2 m of rock above the gouge layer, and it then subsides significantly (the width of the intensely damaged zone may be underestimated because it is much harder to identify those small scale slip surfaces in the stiffer, non-pulverized rock). The exposure extends for about 15-20 m beyond the pulverized zone, depending on the annual water level in the stream and vegetation cover, with a progressively decreasing number of slip surfaces with distance from the fault. The exposure is not continuous further north, although one can get an impression about the subsidence in fracture density and the width of the damage zone by walking northward along a stream-parallel road starting about 15 m above the exposure.

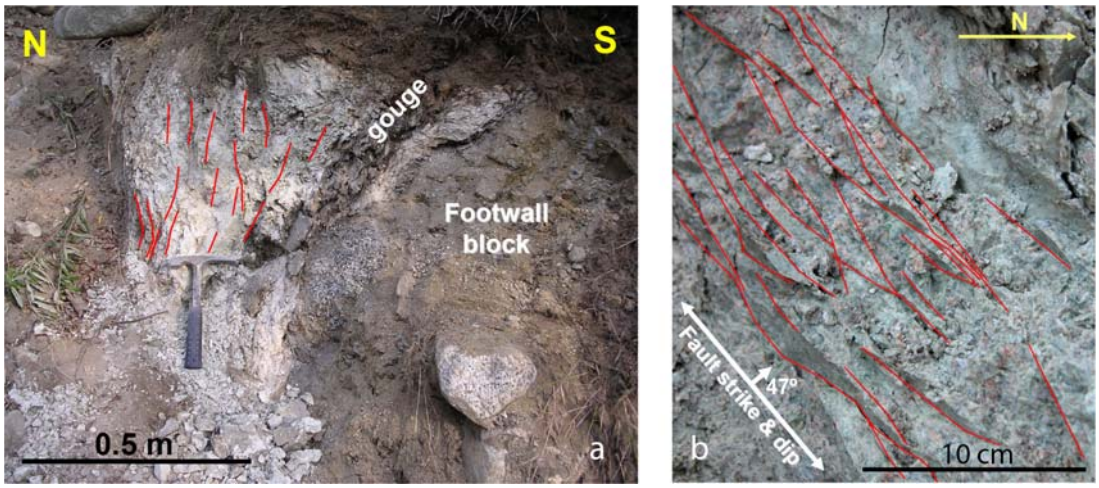

Figure 6: Meso-scale structure of the Sierra Madre fault near JPL. a. Cross fault view: Pleistocene alluvial deposits in the footwall overlaid by ~5 cm thick gouge zone. The granite above the gouge is pulverized. Slip surfaces within the granite are marked with red lines; they are quasi-parallel to the strike of the fault but have a steeper inclination. b. Close up map view of the slip surfaces (red lines).

Figure 6a shows a vertical cross-fault view of the eastern bank of the stream with some of the small slip surfaces delineated. Most strikes are quasi-parallel to the main fault plane but the dips are mostly steeper than that of the main fault. Some slip surfaces dip to the northwest (as does the main fault) while other slip surfaces dip to the southeast. The spacing between these slip surfaces nearest to the main fault is on the order of one cm (Figure 6b), where they exhibit low-angle brunching and coalescence. Many of the surfaces contain a film of gouge that is typically shiny with a silky touch, and almost all of them show slip striations. Some of the slip surfaces are planar and some are curved. Figure 7 shows two relatively small slip surfaces in a typical geometry with their slip striations at a high angle to each other.

Figure 7: Small-scale slip surfaces**.** Note the different sense of curvature, different attitude and different trend and plunge of slip striations (black lines). A very thin gouge layer covers the surfaces. The original granitic fabric, including individual crystals, can be identified in the rock between the surfaces. The rock appears to be intact but it can be easily powdered by hand.

We measured the dip angle and direction of 115 slip surfaces at distances up to about 3 m from the main fault plane, and the trend and plunge of slip striations on them. The sense of motion was inferred for 49 surfaces. The average strike for the slip surfaces (eastern hemisphere) is 88° with a standard deviation of 43°. The strike of 64% of the surfaces is within one standard deviation (Figure 8a). Most of the slip surfaces have high inclination angles (Figure 8b). 70 slip surfaces are dipping northward with an average inclination of 69°, standard deviation of 12° and with 62% within one standard deviation. 45 slip surfaces are dipping southward with an average inclination of 73°, standard deviation of 15° and with 80% within one standard deviation.

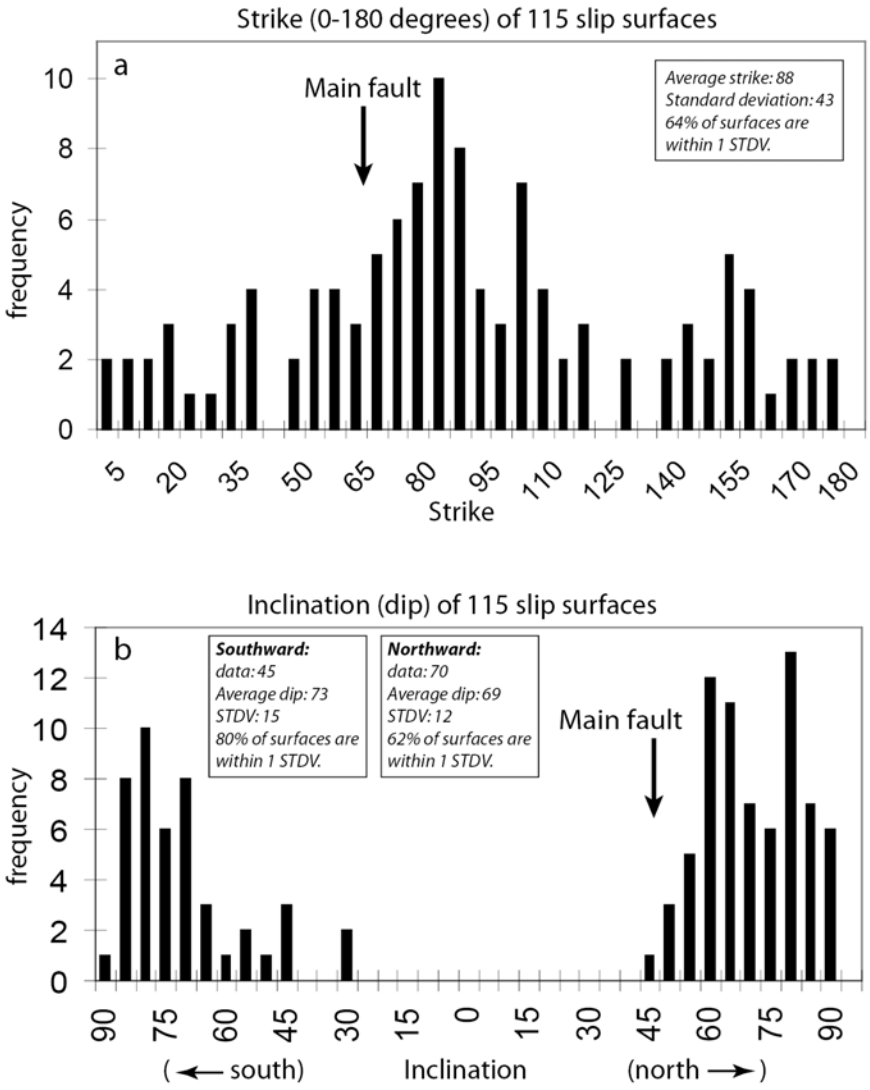

Figure 8: Distribution of strike and dip of slip surfaces, 115 data**.**

The normals to all 115 slip surfaces are plotted in Figure 9a. The sense of motion inferred for 49 slip surfaces is color coded: 36 slip surfaces have a normal sense (red squares) and 13 slip surfaces have a reverse sense (green squares). Despite potential mistakes in the interpretation of kinematic indicators on the surfaces, the preference for a normal sense of motion within this population of slip surfaces is vigorous. The orientation in space of all the slip striations is plotted in Figure 9b, with their plunge

ranging 30°-90° and without a preference for trend (i.e. there is no preference for right or left lateral horizontal component of motion in the data).

In summary, the population of slip surfaces is characterized by a preference for steep inclinations, trend that is oblique, in an acute angle, to that of the main fault, preference for normal faulting and an intermediate to high angle slip vectors.

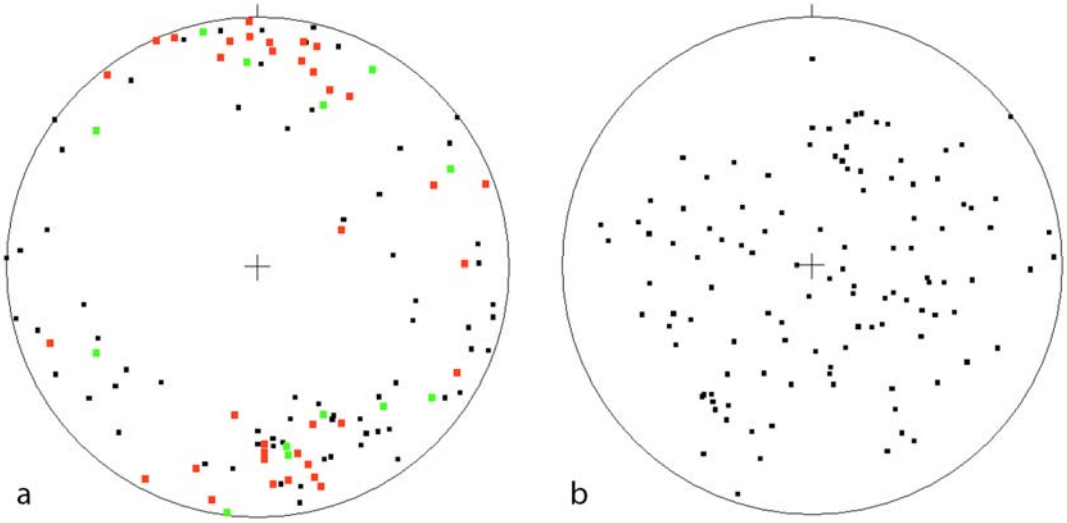

Figure 9: Lower hemisphere equal area projections of normals and slip vectors**.** a. Normals to all 115 slip surfaces. Slip surfaces with identified sense of motion are color coded with red for normal and green for reverse. b. Plunge and trend of all slip striations.

Microscale observations

Sample 183 was extracted from an outcrop of a relatively intact rock with only large, sparse fractures. On the microscale the rock appears to be slightly metamorphosed with over 50% feldspar crystals, >5% micas and the rest quartz. Crystal size is on the mm scale. Although relatively far from the fault, this sample contains many intracrystalline and intercrystalline fractures that are mostly open. Alteration and re-crystallization is minor and shear at this scale appears to be completely absent. All other samples, as suggested by their composition, are damaged products of this rock type.

Samples 0.7 to 9.7 share similar features although the distortion of original rock fabric becomes more intense closer to the fault. Shear bands with opaque fine material or re-crystallized material appear in all of them. Despite strong alteration and shear associated with the shear bands, the original crystals and crystal boundaries are mostly preserved. All the samples show intense intracrystalline and intercrystalline fracturing.

Sample 0, collected immediately above the fault plane, display the following features (Figure 10): the fault gouge is about 2-4 mm thick, containing sparse white visible sub-rounded to angular fragments up to ~100 μm wide. The rest of the gouge material is dark brown to reddish-brown in color and is opaque in an optical microscope. Variations in colors express clear Riedel shears consistent with the sense of motion on the fault. The gouge has a very sharp textural and mechanical boundary with a highly damaged layer immediately above it. This layer is matrix supported with matrix color ranging from black to light brown. Numerous shear bands cross this layer, usually containing ultra-fine dark material. Most of the shears are parallel to the fault. Particle sizes range from the minimum optically visible size to a rare size of about 500 μm. Most of the visible particles are part of clusters in which their shapes fit together with the shapes of other visible particles like pieces of a puzzle. Those clusters appear to be grains that were apparently shattered in-situ without distortion of the grain's shape (observed best under reflected light; see Figure 13a below). This is somewhat surprising given the intense shearing that the layer appears to accommodate.

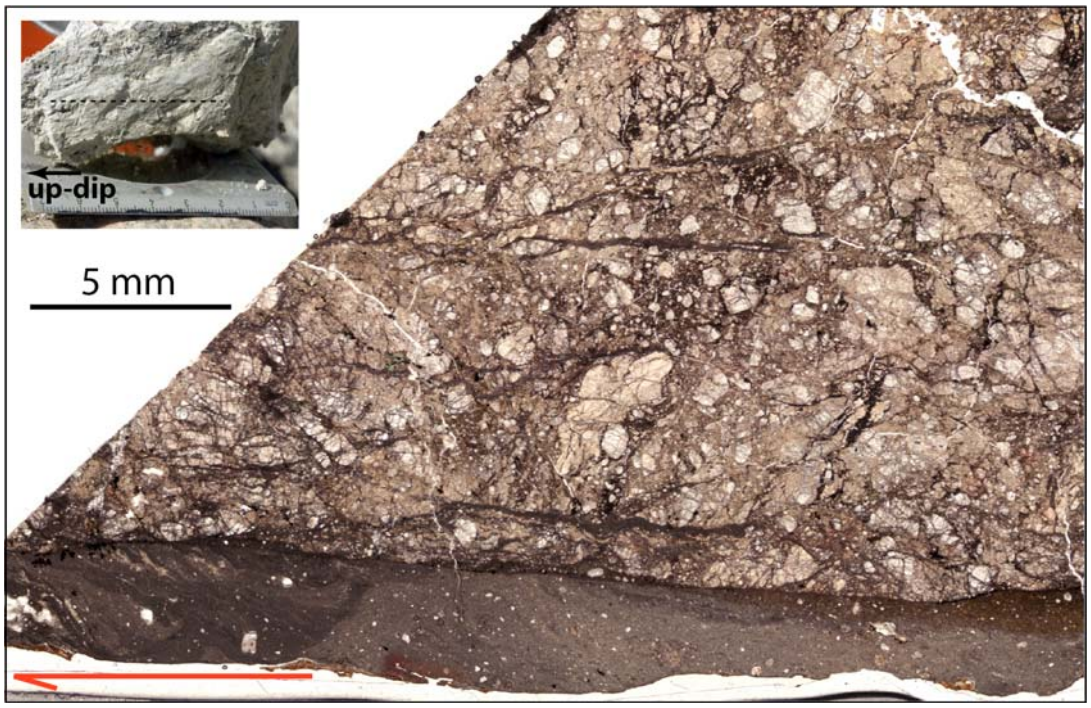

Figure 10: A transmitted light photomicrograph of sample 0. The inset shows the sample, with the gouge layer and slip striations facing toward the viewer, scale in cm. The thin section plane is parallel to the down-dip direction of the fault and it intersects the face of the sample along the black dashed line in the inset. A 2-4 mm wide gouge layer at the bottom of the figure has a sharp mechanical and compositional boundary with the damaged rock above it. Clear Riedel shears compatible with the sense of motion (red arrow) appear inside the gouge. The damaged rock contains many shattered grains supported by a brown opaque highly sheared matrix with some apparent shear bands parallel to the fault.

Figure 11 shows transmitted light photomicrographs of samples 4 and 183 overlaid by a transgranular fractures map. In sample 183 (Figure 11a) all the fractures are marked with black lines and in sample 4 (Figure 11b) fractures are marked with green and blue lines, corresponding to two preferred orientations we identified. Rose diagrams of all the fractures mapped in samples 183 and 4 appear in Figure 12 and data is summarized in Table 1. Fractures in sample 183, assuming to represent the far-field (or regional) damage fabric, have major and minor preferred orientations (Figure 12a): the dominant fracture set trends to the NW, and a minor fracture set trends to the NNE. Fractures in sample 4 have two preferred orientations as well (Figure 12 b-c): fracture set A trends to the NW, like the dominant fracture set in sample 183, and fracture set B trends to the ENE. The

ENE trending set and the population of mesoscale slip surfaces (Figure 12d) have a similar preferred orientation.

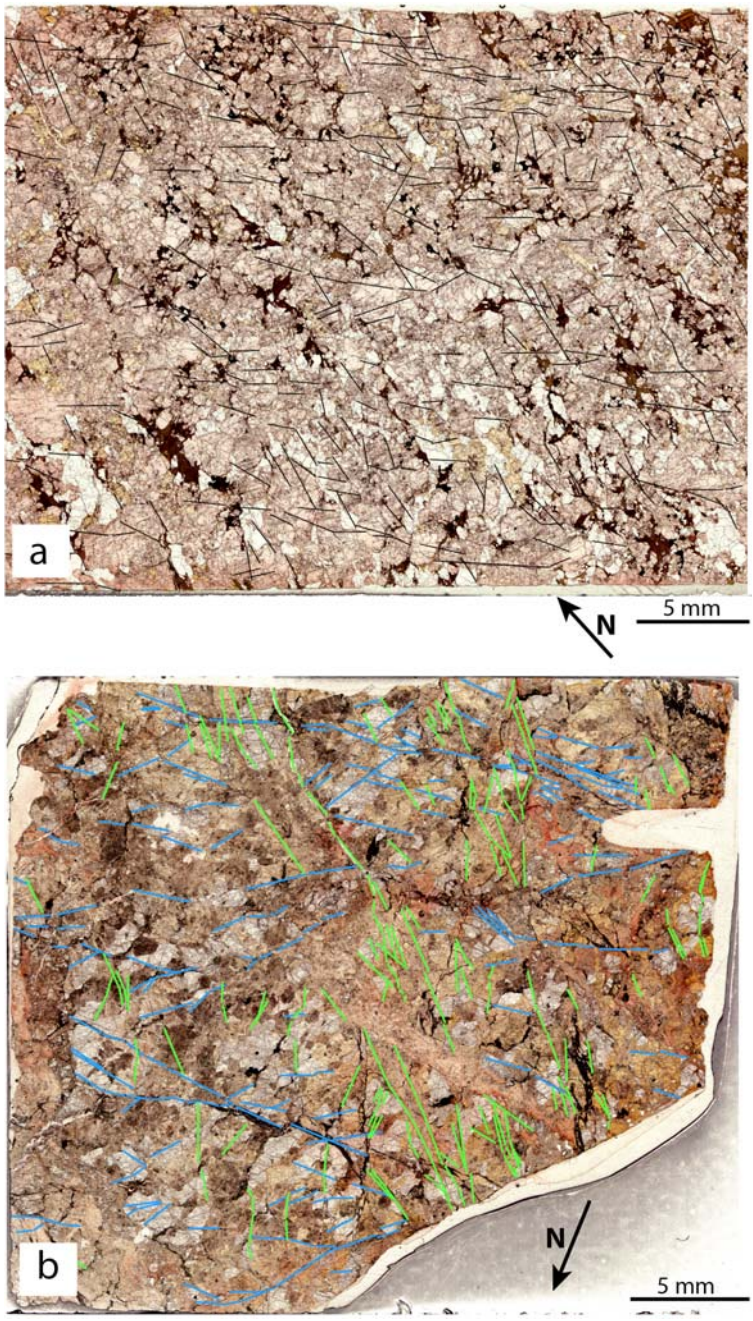

Figure 11: Transmitted light photomicrographs of samples 183 and 4. a. Sample 183, showing an undisturbed crystal-scale and larger magmatic fabric of the granite. Transgranular fractures, marked as black lines, trend mostly to the northwest. b. Sample 4. Original crystal boundaries are largely preserved but the rock fabric is intensely disturbed by several generations of veins, alterations and a dense fracture network. Two sets of transgranular fractures are marked: the green set trends to the northwest, like the dominant fracture set in sample 183; and the blue set trends roughly east-west, similar to the dominant orientation of the mesoscale slip surfaces.

Table 1: Properties of measured fracture sets in samples 183 and 4.

	No. of data	Mean direction	95% confidence interval (+/-degrees)
Sample 183	346	332°	6
Sample 4 – set A	229	322°	5
Sample 4 – set B	192	70°	6

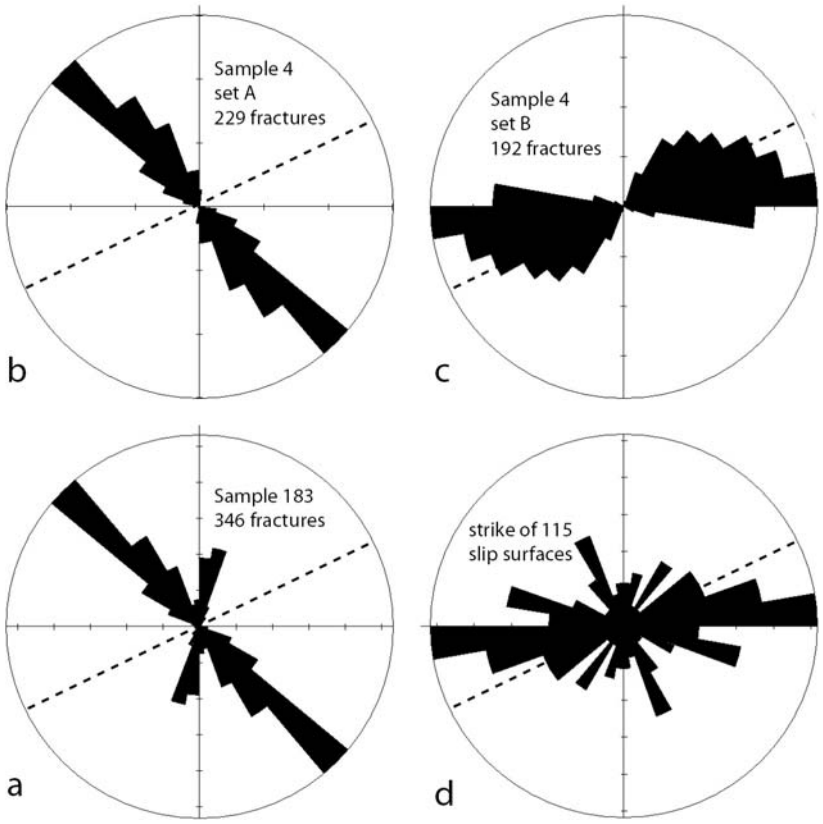

Figure 12: Rose diagrams. a. Sample 183 (Figure 11a), b. Sample 4, set A (Figure 11b, green set), c. Sample 4, set B (Figure 11b, blue set), d. All mesoscale slip surfaces (figures 8, 9). dashed lines represent the orientation of the main fault.

The intensity of fragmentation (shattering) of the crystals intensifies and fragments become smaller closer to the fault. The original crystal outlines are completely preserved in sample 183, and are mostly preserved in sample 4. In sample 0 crystals can still be identified despite the heavy fragmentation, but we observe that their outer shape is more rounded compare to crystals in the other two samples. The average crystal size appears to

be much smaller near the fault compare to the average crystal size in sample 183 (the average size of crystals that we measured in samples 4 and 0 is 49% and 22%, respectively, of the average crystal size in sample 183. Note that this is not the average *grain size*). The more rounded shapes of crystals in sample 0, compare to the irregular shapes of crystals in the other samples, can probably be attributed to wear, rotation and shearing. In addition, fragments in sample 0 seem to have a higher aspect ratio compare to fragments in the other two samples (Figure 13). They still have sharp corners and they fit very well with neighboring fragments, suggesting minimal shear of the individual crystals. The more intense fragmentation near the fault is expected, but the different fragments shape near the fault is intriguing, suggesting that the grain size reduction mechanism operating in sample 0 is unique to the vicinity of the fault plane.

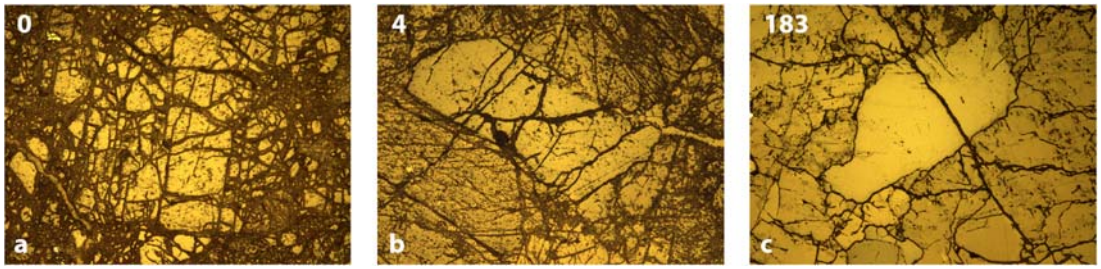

Figure 13: Photomicrographs of single grains. Samples names / distances from the fault appear in the upper left corner of each image. a. Sample 0: the crystal, embedded in a cataclastic matrix, is strongly shattered but its fragments still fit together. Aspect ratio of fragments is high. b. Sample 4: quartz crystal (lighter color) cut by few transgranular and intragranular fractures. c. Sample 183: quartz crystal, cut by a single transgranular fracture.

Discussion

Activation of cm-scale slip surfaces during earthquake ruptures

A strike-slip fault along with two subsidiary slip surfaces in the general geometry predicted by Rice et al. (2005) (e.g. Figure 1b) for Coulomb failure outside the fault plane is projected on a lower hemisphere net in Figure 14a. These elements are projected twice: as planes and as normals to these planes. The fault plane and its normal are projected with thick line and thick open circle, respectively, and the slip surfaces and their normals are projected with thin lines and thin open circles, respectively. A projection of the slip vector on the main fault is shown with a filled circle. This geometry implies that the normals to the slip surfaces, the normal to the main fault surface and the slip vector on the main fault lie on the same plane.

Assuming Andersonian faulting conditions, the fault dip (47°) is also its angle with the maximum pre-stress direction. On the basis of detailed boreholes data, trenching and surface mapping in and around our study area, Crooks et al. (1987) indicate that “the fault zone consistently dips about 45° N”. Here we compare our observations with a simulation by Rice et al. (2005) for a case with 45° between the fault and the maximum pre-stress direction.

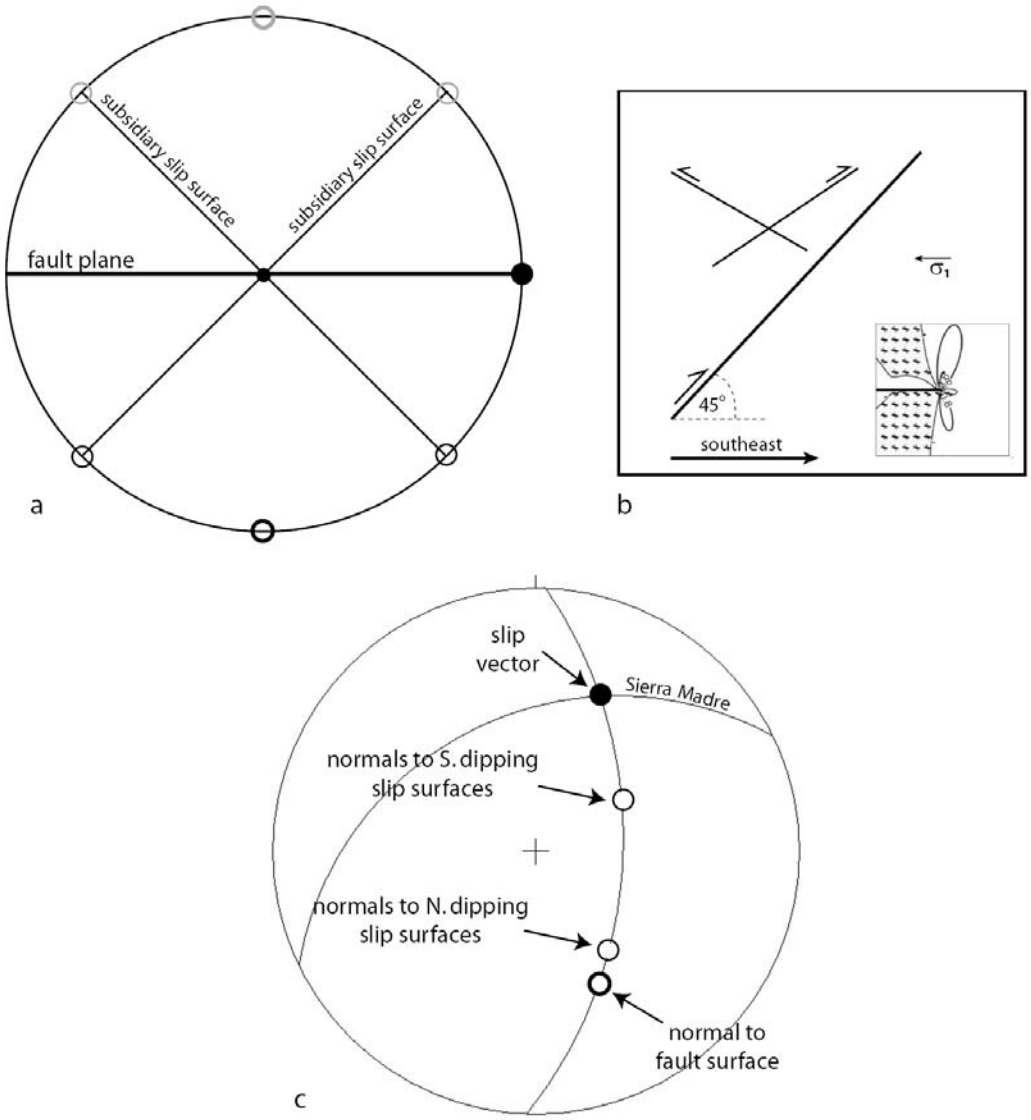

Figure 14: Projection of model prediction on the Sierra Madre fault geometry. a. Lower hemisphere projections of a strike slip fault and the associated generic damage geometry predicted by Rice et al. (2005). See Figure 1b here. The main fault surface is projected as a thick line and its normal is projected as a thick circle. The slip vector is projected as a filled circle. Slip surfaces are projected as thin lines and their normals are projected as thin circles. Since those elements are vertical, their normals could be projected also as the gray circles at the top. The normals to the slip surfaces must be contained in the plane that includes the normal to the main fault and its slip vector. b. A fault and the exact geometry for preferably oriented slip surfaces activated due to Coulomb yielding associated with off-fault dynamic stresses for a case of 45° between the fault and the maximum pre-stress direction. This is a simplified graphic version of the fault and two slip surfaces as they appear in a simulation shown in Figure 12 of Rice et al. (2005) (in the inset; legend is similar to that of Figure 1b). The fault and the two slip surfaces were rotated to represent a vertical cross section of a thrust fault. Only slip surfaces on the side of the fault that corresponds to the hanging-wall are shown. c. Lower hemisphere equal area stereographic projection of the Sierra Madre fault and the plane containing the fault slip vector (filled circle) and the normal to the fault (thick circle). The predicted favorably oriented slip surfaces from (b) are projected as thin circles.

For an up-dip mode II rupture in such a case and under some conditions - high rupture speed, large residual stress ratio, short slip weakening distance and non-zero poroelastic effects - the Mohr-Coulomb failure criterion is exceeded on the side of the fault that corresponds to the hanging wall of a thrust fault (our observations are made in the hanging wall of the fault and we assume up-dip rupture propagation for past earthquakes). The results of this simulation appear in Figure 12 of Rice et al. (2005), shown here as an inset in Figure 14b. According to the simulation, the subsidiary slip surfaces that will be activated have a favorable orientation with respect to the main fault surface of 13° and 77°. In reality, it is expected that surfaces in a range of orientations centered on the favorable orientations will be activated. Figure 14b simplifies the simulation results by showing only the main fault and two subsidiary slip surfaces at 13° and 77° with respect to the fault. Both the original figure from Rice et al. (2005) and Figure 14b here show a cross section of the faults with their strike perpendicular to the plane of the page. The two slip surfaces shown in Figure 14b have an opposite sense of motion: if this cross section is viewed as a map, the surface oriented at 13° to the main fault is right lateral and the surface oriented at 77° is left lateral. The fault and the slip surfaces are rotated so it is equivalent to a cross section of the Sierra Madre fault in its true inclination. In this configuration the two simulated slip surfaces with opposite sense of motion are both reverse faults.

Figure 14c shows the prediction of the Rice et al. (2005) model for the conditions above on the projected geometry of the Sierra Madre fault and for ruptures propagating in the direction of the slip vector found in our working location. Since the fault is dipping 47° to 334° with a slip vector plunging 35° to 023°, the plane that contains the slip vector

and the normal to the fault is dipping 63° to 092°. Application of the simulation results for the Sierra Madre fault requires that this plane contain the normals to the favorably oriented slip surfaces predicted for reactivation, i.e. normals to surfaces at 13° and 77° with the fault plane. In the projection the normals to these slip surfaces must lie on the line that represents this plane, and they are represented in Figure 14c as open circles.

We overlaid the predicted geometry of slip surfaces as shown in Figure 14c on our contoured data set of normals to the observed slip surfaces (Figure 15). Like the normals to the *predicted* slip surfaces, the peaks in the distribution of normals to the *observed* slip surfaces (blue counters) lie on the plane containing the normal to the main fault plane and its slip vector. If the observed slip surfaces were formed in the predicted geometry, they must have been rotated to their current inclination.

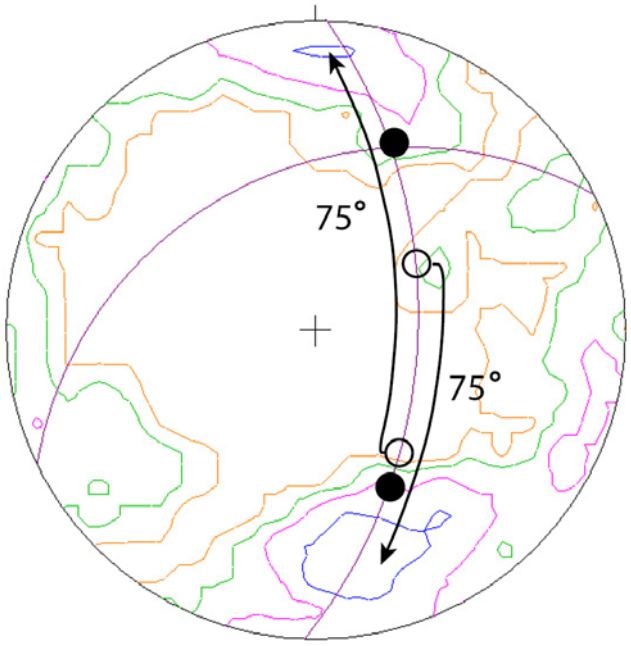

Figure 15: The contoured data set of 115 normals to slip surfaces projected over the prediction of Figure 14c. The peaks in the distribution of the normals (blue contours) lie on the plane containing the normal to the fault, its slip vector, and the normals to the predicted favorably oriented slip surfaces. A rotation of 75° around as axis normal to that plane of those predicted surfaces in the directions allowed by their sense of slip (Figure 14b) brings them to the orientation of the observed slip surfaces. The rotation in the figure does not appear to be identical for the two predicted surfaces due to a visual effect.

Due to the sense of motion on the predicted slip surfaces (see Figure 14b), the predicted south-facing slip surfaces can only be rotated clockwise and the predicted north-facing slip surface can only be rotated counterclockwise. Trying various rotation angles for those slip surfaces around an axis perpendicular to the plane containing the normal to the main fault surface and its slip vector, we found that rotating *both* predicted slip surfaces 75° in the *allowed* directions (Figure 15), shift their projected normals to the peak (blue contour) in the distribution of the observed slip surfaces. The result of this rotation is shown in Figure 16: both predicted-rotated slip surfaces are now dipping in a steep inclination, about 30° steeper than the fault surface itself, similar to the geometrical relationships observed in the field (compare to Figure 6 and data in Figures 8, 9, 12 and 15). In addition, both predicted slip surfaces, which had a reverse sense of motion in their original inclination, have a normal sense of motion in their rotated inclination, compatible with our observation of preference for a normal sense of motion in the data (see Figures 8 and 9). Scattering in the inclinations, as shown schematically in Figure 16 by the thin dashed lines, will allow some of the slip surfaces to maintain their reverse sense of motion.

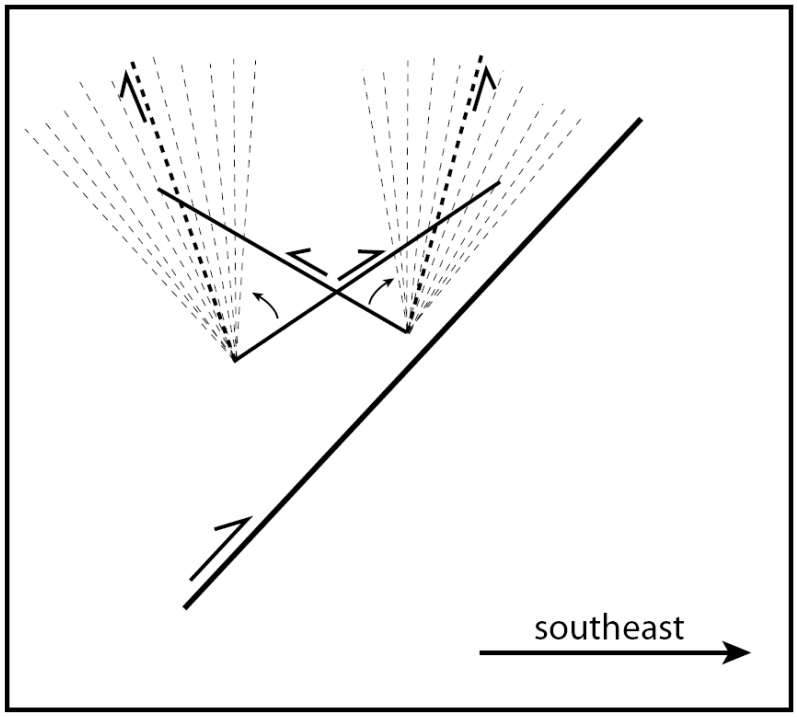

Figure 16: Rotated predicted data compared with observed data**.** The predicted slip surfaces of Figure 14b (thin continuous lines) rotated 75° in the direction allowed by their sense of motion (dashed thicker lines). The resultant geometry is similar to that observed in the field (Figure 6a), with a preference for normal faults, as shown in the data (Figure 9a). A scattering in the original dip angles of the slip surfaces population will allow some of the rotated slip surfaces (thin dashed lines) to maintain their reverse sense.

Large rotation of closely spaced conjugate sets of slip surfaces, at the order of the rotation inferred for our case, should be associated with displacement of surfaces by each other and fragmentation of the rock between the slip surfaces into smaller blocks with rounded faces (especially if the rock is soft or pulverized), and this is what we observe in the 1-2 m of rock above the fault plane. As we get closer to the fault surface, especially in the 0.5 m immediately above it, the slip surfaces create an anastomosing web of surfaces that bound rock fragments with concoidal shapes (as in Figure 7). The size of the slip surfaces becomes smaller as they are more closely spaced. This geometry is compatible with an internal rotation of the rock mass. As the rotation-fragmentation progress, the original slip surfaces architecture is obliterated, and the small fragments may experience

different kinematics than the one described above for the slip surfaces. In our measurements we therefore avoided particularly small surfaces with concoidal shapes (at the order of ~2 cm, e.g. Figure 7) and chose larger and more planar surfaces that 'survived' the rotation.

Under ideal conditions where successive rupture events propagate with the same slip vector on a perfectly planar fault surface we would expect minimal scattering in the orientation of the subsidiary slip surfaces and their slip vectors. A common observation in natural faults is crosscutting relations between sets of slip striations (e.g. Sagy et al., 2007), sometimes during a single slip event (Nobuaki and Kenshiro, 2003). Given that the slip vector may change between rupture events and even during the propagation of one rupture, changes are expected in the configuration of the off-fault stress field and the resulting favorable orientation of activated slip surfaces. It is therefore surprising to find sets of slip surfaces with preferred orientation, but this is what we observe. The existence of such identifiable sets implies that the slip vector on this fault was relatively uniform throughout its displacement history. The large scattering in the orientation of the slip vectors (Figure 9b) may be partially the result of variations in the off-fault stress field and partially due to exhumation and un-roofing of the fault. When the rock mass approaches the surface, it becomes more susceptible for strain due to thermal cycling, which may activate slip on existing slip surfaces. This non-tectonic process may affect the distribution of the slip striations data. Nevertheless, the slip vectors for the slip surfaces predicted by the model for our case are expected to lie on the plane containing the normals to the slip surfaces, the normal to the fault and its slip vector. Since this plane has high inclination (Figure 14c) and the slip surfaces are generally steep, the slip vectors

are expected to have a relatively high inclination too. The slip vector data set in Figure 9b is compatible with this prediction, showing a preference for intermediate to high inclination angles.

Microfractures and pulverization

The two distinct sets of fractures mapped in sample 4 can be interpreted in a mechanical framework: fracture set A, trending to the northwest, is similar in its orientation to the dominant fracture set found in sample 183 (Figure 12a, b). Those sets are perpendicular or nearly perpendicular to the fault strike. Their density seems to be similar between the two samples (although not considered here as a fracture density measurement, the number of fractures belong to those sets is very similar between the samples, given that the area of the thin section of sample 4 is 2/3 the area of the thin section of sample 183. As of graphic reasons some of the image area of sample 183 is cropped in Figure 11). Since this fracture orientation appears both near and far from the fault without an apparent drop in the fracture density, this orientation is probably a representative of the regional fracture fabric, which is compatible with northwest-southeast compression. Such a compression direction is expected if the Sierra Madre fault is operating under Andersonian faulting conditions, with the maximum compressive stress horizontal and normal to the fault strike. This supports our assumption of Andersonian conditions when applying the Rice et al. (2005) model for the Sierra Madre fault. Fracture set B (Figure 12c) shares similar orientation with the average trend of the mesoscale slip surfaces (Figure 12d), and is most likely associated with their formation (e.g. Moore and Lockner, 1995).

Another aspect of the damage observed in the microscale is that transgranular and intragranular fractures reduce the grain size without distortion of the original crystals shape, while larger scale shear bands and veins dissect the rock and disturb magmatic fabrics. These damage elements are observed in all samples between 9.7 and 0.7 m from the fault, with increasing intensity toward the fault. The damage pattern in sample 0 immediately above the fault plane appears to be different with much denser intragranular fracture network, breaking crystals to much smaller fragments with higher aspect ratio (Figure 13). The crystals are apparently smaller and more rounded compare to crystals in samples further away from the fault, and they are embedded in a fine, highly sheared cataclastic matrix.

The association of both cataclasite and shattered but apparently not distorted grains suggests the operation of both shear of the bulk rock and failure of individual grains under tension. While intense shear and cataclastic flow is expected immediately near the fault surface, tensile regime is less intuitive in such an environment. One mechanism that can lead to failure due to a grain-scale tensile stress in a compressive environment is failure under bi-polar loading by same-sized neighbors in the load-bearing stress chains that transmit force in a granular media (e.g. constrained comminution, Sammis et al., 1987). This process is not unique to dynamic rupture and should result in grain size distribution with fractal dimension of 2.6 or 3, depending on the matureness stage of the fault (Sammis and King, 2007). Another possible source for tensile stresses associated with earthquake ruptures is fault normal unloading and loading i.e., an opening mode (Brune et al., 1993) that may lead to a complete reduction of the normal stress. Such an opening mode is expected to be especially pronounced in the hanging-wall of a thrust

fault, and in particular as the rupture approaches the surface near the fault toe (Brune, 1996; Shi et al., 1998; Oglesby et al., 1998, 2000). The shattered crystals in sample 0 and the overall pulverization with minimal distortion of fine magmatic fabrics further away from the fault surface could be the damage products of such an opening mode. While it is difficult to resolve which of the two mechanisms is responsible for grain-scale failure under tension, we note that failure is likely associated with dynamic rupture.

Damage accumulation over many seismic cycles

As mentioned above, the existence of identifiable preferred orientation in the population of slip surfaces, if those were indeed activated as a response to off-fault dynamic stresses, suggests that the fault slip vector did not change significantly during and between rupture events. This is surprising because during the fault history the roughness of the fault and the fault interaction with other faults, layers and various structural heterogeneities should cause stress perturbations both static and dynamic. These are expected to influence the fault's kinematics, e.g. lead to changes in the slip vector both temporally and spatially. Another intriguing observation is that only one conjugate set of slip surfaces was developed (although the scattering in the data may suggest the immature development of an additional set). After significant rotation the orientation of the slip surfaces should have become unfavorable for activation. Upon further faulting, the development/activation of an additional set of surfaces is expected. This did not happen or happened in a very minor form. It is therefore likely that the observed architecture of slip surfaces developed over a finite (short) displacement history in which faulting conditions remained stable. Activity of the slip surfaces then ceased,

and their fossilized architecture was exhumed. Alternatively, the conditions required for the activation of the surfaces are met only at some interval along the fault surface at depth (for example, high rupture velocity, specific poroelastic conditions etc.). When the rock mass containing those slip surfaces propagates up-dip, the conditions then become insufficient for their activation – and their fossilized architecture is exhumed while at depth the process continues.

We note that the stress field required for the activation of the favorably oriented slip surfaces and an opening mode with complete reduction of the normal stress are unlikely to operate simultaneously. However, if a rock mass containing the fossilized slip surfaces architecture approached the surface and was then subjected to an opening mode, since the later is predicted to operate very strongly at shallow depths and in particular in the fault toe, the signature of the two mechanisms could be found together.

We conclude that the observed slip surfaces in the few meters above the fault surface were probably activated when the Mohr-Coulomb yielding criterion was exceeded during ruptures propagation (Rice et al., 2005), while pulverization immediately above the fault surface could possibly be related to a dynamic opening mode.

Summary

We identified that the following processes may have operated in the hanging-wall of the Sierra Madre fault:

1. Mohr-Coulomb Slip on- and rotation of small scale favorably oriented cm-scale slip surfaces in a few meters zone above the fault surface during the passage of earthquake ruptures.

2. Development of fracture fabric in the few meters above the fault surface associated with the generation of the mesoscale slip surfaces.
3. Development of fracture fabric on a regional scale associated with compressive stresses in an Andersonian geometry with respect to the fault surface.
4. Cataclastic process in a few cm wide layer immediately above the fault plane, leading to strong grain size reduction and shearing of the rock.
5. In-situ fragmentation of crystals without significant shape distortion in the cataclastic layer immediately above the fault surface. This could possibly be the result of tensile stresses associated with dynamic opening mode.
6. Riedel shears and extreme grain size reduction within mm scale wide gouge layer.

References

Blythe, A.E., Burbank, D.W., Farley, K.A. and Fielding, E. (2000). Structural and topographic evolution of the central Transverse ranges, California, from apatite fission track, (U/Th)/He and digital elevation model analyses. Basin Research., 12, 97-114.

Brune, J. N., Brown, S. and Johnson P.A. (1993). Rupture mechanism and interface separation in foam rubber models of earthquakes; a possible solution to the heat flow paradox and the paradox of large overthrusts. *Tectonophysics.,* 218, 1-3.

Brune, J. N. (1996). Particle motion in a physical model of shallow angle thrust faulting, *Proc. lndian. Acad. Sci.* 105, 197-206.

Crook R. Jr, C.R. Allen, B. Kamb, C.M. Payne, and Proctor R.J. (1987). Quaternary geology and seismic hazard of the Sierra Madre and associated faults, western San Gabriel Mountains - US Geological Survey Professional Paper.

Doblas, M. (1998). Slickenside kinematic indicators. Tectonophysics., 295, 187-197.

Dor O., Ben-Zion, Y., Rockwell, T.K., and Brune J.N. (2006). Pulverized Rocks in the Mojave section of the San Andreas Fault Zone, *Earth Planet. Sci. Lett.* 245, 642-654. doi:10.1016/j.epsl.2006.03.034.

Monzawa, N. and Otsuki, K. (2003). Comminution and fluidization of granular fault materials: implications for fault slip behavior. Tectonophysics Volume 367, Issues 1-2, 29 May 2003, Pages 127-143. doi:10.1016/S0040-1951(03)00133-1

Moore DE, Lockner DA (1995). The role of microcracking in shear-fracture propagation in granite. J Struct Geol 17:95-114.

Oakeshott, G.B. (1971). Geology of the epicentral area. Calif. Div. Mines Geol. 196, 19-30.

Oglesby, D. D., R. J. Archuleta, and S. B. Nielsen (1998). Earthquakes on dipping faults: the effects of broken symmetry, *Science* 280, 1055–1059.

Oglesby, D. D., R. J. Archuleta, and S. B. Nielsen (2000). Dynamics of dip-slip faulting: explorations in two dimensions, *J. Geophys. Res.*105, 13,643–13,653.

Poliakov, A. N., B. R. Dmowska and J. R. Rice (2002). Dynamic shear rupture interactions with fault bends and off-axis secondary faulting, *J. Geophys. Res*., 107, B11, doi:10.1029/2001JB000572.

Rice, J. R., Sammis, C. G. and Parsons, R. (2005). Off-fault secondary failure induced by a dynamic slip pulse. *Seismol. Soc. Am. Bull*., 95, 109-134.

Rubin, C., Lindvall, S. and Rockwell, T.K. (1998). Evidence for large earthquakes in metropolitan Los Angeles. Science., 281. 298-402.

Sagy A, Brodsky EE, Axen GJ (2007) Evolution of fault-surface roughness with slip. Geology: Vol. 35, No. 3 pp. 283–286.

Sammis, C.G., King, G.C. and Biegel, R.L. (1987). The Kinematics of Gouge Deformation, *Pure and Appl. Geophys*.125, 777–812.

Sammis, C. G. and King, G. C. (2007). The Mechanical Origin of Power Law Scaling in Fault Zone Rock. *Geophys. Res. Lett*., in review.

Shi, B., A. Anooshehpoor, J. N. Brune, and Y. Zeng (1998). Dynamics of thrust faulting: 2-D lattice model, *Bull. Seism. Soc. Am.* 88, 1484–1494.

Tucker, Allan Z., Dolan, James F. (2001). Paleoseismologic Evidence for a >8 Ka Age of the Most Recent Surface Rupture on the Eastern Sierra Madre Fault, Northern Los Angeles Metropolitan Region, California. Bulletin of the Seismological Society of America. 91: 232-249.

Bibliography

Dor, O., C. G. Sammis, and Y. Ben-Zion, The geometry of slip surfaces in the hanging-wall of the Sierra Madre fault, La Canada, California: evidence for Mohr-Coulomb failure induced by a dynamic off-fault stress field, to be submitted to Pure and Applied Geophysics, 2010.